Computational Materials Science 262 (2026) 114369

Contents lists available at ScienceDirect

Computational Materials Science

journal homepage: www.elsevier.com/locate/commatsci

Full length article

Angular-dependent interatomic potential for large-scale simulation of bcc and hcp multi-component refractory alloys

Sergei Starikov [a,*], Petr Grigorev [b], Sang-Hyeok Lee [c], Zhuocheng Xie [c], Pär A.T. Olsson [d,e]

[a] ICAMS, Ruhr-Universität Bochum, 44801 Bochum, Germany
[b] CNRS, INSA Lyon, Universite Claude Bernard Lyon 1, MATEIS, UMR5510, 69621 Villeurbanne, France
[c] Institute for Physical Metallurgy and Materials Physics, RWTH Aachen University, 52074 Aachen, Germany
[d] Materials Science and Applied Mathematics, Malmö University, SE-205 06 Malmö, Sweden
[e] Division of Mechanics, Materials and Component Design, Lund University, Box 118, SE-221 00, Lund, Sweden

ARTICLE INFO

Keywords:
Refractory metals
Interatomic potential

ABSTRACT

This work is devoted to the development and comprehensive validation of a new interatomic potential for bcc and hcp refractory alloys based on the W–Mo–Nb–Ta–Zr–Ti system. The presented model allows the simulation of various structural transformations, as well as the behavior of crystal defects in several of the phases observed in this system. The classical form of the potential enables simulations of atomic systems comprising up to 10^8 atoms for durations longer than a million time steps using a routine computational setting. The wide applicability of the developed model is demonstrated by the example of studying phase transformations in Ti–Nb alloys and the properties of defects in Laves phases.

1. Introduction

Refractory metals (RMs) play an important role as structural materials in various fields of materials science [1–3]. Because of their exceptional high-temperature strength, as well as their resistance to wear and erosion, refractory alloys (RAs) are extensively used in applications ranging from jet engines and rocket nozzles to nuclear reactors, furnace components, and medical devices. In recent decades, particular attention has been paid to the study of complex concentrated refractory alloys (CCRAs) due to their exceptional mechanical properties at high temperatures [4,5] and the increasing interest of studying high-entropy alloys [6,7]. Many recent studies have focused on the behavior of crystal defects and structural transformations in these alloys, as such phenomena are central to understanding the overall material properties. In this case, atomistic simulation can provide powerful insights into the mechanisms of various processes related to the crystal defect properties. Thus, the development of reliable interatomic models for CCRAs is of crucial importance for this line of research, since the efficiency and predictability of classical atomistic simulation is dictated by the choice of the interatomic potential [8–10].

Several reliable interatomic potentials have been developed for traditional RAs within the W–Mo–Nb–Ta system [11–15]. However, for RAs with a broader definition – including Ti and Zr – interatomic potentials are still lacking. This can be partly explained by the increased complexity of the properties of Ti and Zr metals compared to traditional cubic RMs. The main crystalline phase of traditional RMs is a body-centered cubic (bcc) structure, and no significant phase transformations occur in these alloys, except for the order–disorder transition that occurs in CCRAs [16,17]. In contrast, for pure Zr and Ti alloys, several structural transformations may occur, and a number of intermetallic compounds can be stabilized in RAs by the addition of such metals. Some classical potentials have been proposed for such systems and are commonly used [18–20]; however, their predictability is limited because of the heuristic mixing scheme for alloys. To the best of our knowledge, no reliable interatomic potential has been proposed for the W–Mo–Nb–Ta–Zr–Ti system, aside from some universal machine-learning (ML) models [21–23], which today remain prohibitively expensive for large-scale atomistic simulations involving more than 10^4 atoms. Although such universal models represent powerful computational tools, many problems in materials science routinely demand atomistic simulations on the order of 10^5–10^7 atoms [24,25]. The development of a classical interatomic potential for such a six-element system is the main goal of this work.

* Corresponding author.
E-mail address: sergei.starikov@icams.rub.de (S. Starikov).

https://doi.org/10.1016/j.commatsci.2025.114369
Received 4 October 2025; Received in revised form 3 November 2025; Accepted 3 November 2025
Available online 6 November 2025

2. Development details

The new potential proposed in this paper has the form of an angular-dependent potential, which will hereafter be referred to as ADP. In our previous paper, we have already developed an ADP for the W–Mo–Nb system [26]. The previously obtained potential functions for this ternary system are incorporated in the new six-element potential with minor modifications. Thus, here we present the main characteristics that are important for the development and validation of ADP functions for Ta, Zr, and Ti metals, and other alloys outside the W–Mo–Nb system. Many results of validation tests of the ADP potential for W–Mo–Nb can be found in various articles [24–26] and the Supplementary Material documents [27] connected to this work, in which we briefly repeat some of the tests for ADP and other interatomic models.

The ADP class of interatomic potentials was proposed by Mishin et al. [28] as an extension of the widely used EAM formalism. For a six-element system, the ADP contains 75 potential functions, each represented with cubic splines. Typically, the ADP model is only two to three times slower than the most efficient EAM potentials [29], making it suitable for large-scale molecular dynamics (MD) simulations. In this work, the potential functions were determined using the force matching method [30] with the potfit code [31,32]. This method provides a rigorous way to construct physically justified interatomic potentials based on a large fitting database containing only results of Density Functional Theory (DFT) calculations. The idea behind this approach is to adjust the interatomic potential functions to optimally reproduce per-atom forces (together with total energies and stresses) computed at the ab initio level for a fine-tuned set of reference structures. A simulated annealing algorithm, serving as a global stochastic optimization method, was employed to explore the parameter space of the interatomic potential and identify the optimal parameter values. Some details of this method can be found in our previous papers, where we used this technique to develop ADP potentials for Fe–Cr–H [33], Si–Al–Au [34] and W–Mo–Nb [26].

DFT calculations for the dataset preparation were performed using the VASP code [35] (version 5.4.4). The calculations were carried out within the generalized gradient approximation (GGA) using the Perdew–Burke–Ernzerhof (PBE) parametrization of the electron exchange–correlation functional. The projector augmented-wave (PAW) method was used to describe the wave functions close to the core. The cut-off energy of the plane-wave basis set was equal to 550 eV.

In addition to the previous 327 configurations from the work for the W–Mo–Nb potential [26], the reference dataset included 643 new configurations representing the W–Mo–Nb–Ta–Zr–Ti system. Each configuration consisted of approximately 250 atoms in a simulation box with periodic boundary conditions. All configurations were obtained from classical atomistic simulations (MD or static) using the potentials [18,26,36]. The complete dataset includes various bulk phases (solid, liquid) and crystal defects of pure metals and alloys of varying composition. In total, the new reference DFT database included 970 energy values, 5412 stress tensor values and 435 354 values of the force components. The dataset is available in NoMaD dataset repository [37, 38].

The root-mean-square error of the ADP prediction estimated with respect to the entire DFT database is about 615 meV/Å for all atomic forces, and 259 meV/Å when only the considering configurations with force components smaller than 5 eV/Å. The average energy error for the entire dataset is 53 meV/atom. The relatively large force error obtained for the entire dataset arises from the fact that fixed potential functions were used for the W–Mo–Nb part [26]. However, detailed information on the force errors for the various datasets, presented in the Supplementary Materials [27] and in the following section, confirms that the developed ADP potential exhibits accuracy comparable to that of other classical potentials and even certain ML model. The developed ADP for the W–Mo–Nb–Ta–Zr–Ti system can be downloaded from the NIST interatomic potentials repository [39,40].

3. Tests with different datasets

Reproducing forces and energies from the reference dataset is a fundamental benchmark for any interatomic potential. Here we tested the new ADP by calculating forces not only in our dataset (ADP-dataset), but also in other DFT datasets available for RAs. Notably, we used three different datasets that were compiled for the development/validation of universal machine learning models: Song-2024 [41], MPTraj [42] and Alexandria [43]. For all datasets, we considered only the W–Mo–Nb–Ta–Zr–Ti part and primarily focused on atomic forces only, to avoid possible issues with energy renormalization. In addition to the ADP, we validated several interatomic models that can also be used, at least partially, to simulate the same system: SNAP [11], TabGAP [14], MTP [12], EAM [18], MEAM [19], three version of MACE (MP-0b3, MPA-0 and MATPES-PBE-0) [44], NEP-2024 [41], NEP89 [45], UMA-S-1 [46] and GRACE-2L-OAM [23]. Table 1 summarizes the calculated errors for atomic configurations with forces below $f < 5$ eV/Å. This force threshold partially excludes highly non-equilibrium configurations; however, some high-energy configurations are presented in these tests. The Supplementary Materials contain test results for all configurations with detailed descriptions. In addition, we have included tests of configuration energies without normalization in the Supplementary Materials [27].

According to the test results shown in Table 1, the force error for ADP is generally of the same order as for the other two classical potentials (EAM and MEAM) and higher than for the ML models. However, it should be noted that MEAM, SNAP, TabGAP and MTP were used here only to test the 4-element system: Nb–Ta–Ti–Zr for MEAM and W–Mo–Nb–Ta for the other three potentials. Thus, direct comparison of ADP is reasonable only for universal ML models. As mentioned above, universal ML models are indeed powerful and accurate tools, with the capability of reproducing DFT data with exceptional accuracy. Among them, GRACE-2L provides the best balance between accuracy and stability (the error is extremely low in all tests). GRACE-2L also demonstrates exceptional accuracy among the ML models for the basic properties of crystal defects in pure metals, see Supplementary Materials [27]. At the same time, ADP provides acceptable error for the datasets, and its main advantage being the ability to describe large atomic systems, as its computational cost is about 10000 times lower than that of universal ML models.

4. Properties of pure metals

We began our primary tests by examining the properties of pure metals. Here we tested only pure Ta, Zr, and Ti, and a complete validation of the W–Mo–Nb part can be found in our previous works [24–26], as well as in the Supplementary Material documents [27]. In addition to ADP, we also tested EAM [18] and MEAM [19] potentials, which are widely used to model the Ta-Zr-Ti system.

Fig. 1 shows the calculated dependence of energy E on atomic volume V for basic crystal structures in the simulated metals: bcc, fcc, A15, hcp and ω-phase (the last two only for Ti and Zr). Along with the simulation results for the aforementioned classical potentials, the figure shows the available DFT data [47,48] for these structures. For Ti and Ta, it can be seen that ADP describes the $E(V)$ dependencies with better accuracy than the EAM and MEAM models. For zirconium, ADP gives acceptable results, but the difference between the fcc and hcp phases is relatively small, as is the case for EAM. One of the most important properties reproduced by the ADP potential is the correct energy difference between the bcc and hcp phases in Ti and Zr. This energy hierarchy plays a crucial role in the simulation of CCRAs with a bcc lattice containing high concentrations of Ti or Zr.

Several recent studies [49,50] have emphasized the important role of delocalized nonlinear vibrational modes (DNVMs) in describing discrete breathers in bcc metals. Following the approach of work [50], we calculated the dependence of the atomic energy on the DNVM

Table 1
Average force error for different interatomic potentials in different datasets for refractory alloys (in eV/Å). Along with the interatomic models, the value in brackets indicates the total number of chemical elements used in the test.

	ADP-dataset	Song-2024	MPTraj	Alexandria
ADP (6)	0.26	0.56	0.43	0.37
EAM (5)	0.45	0.53	0.43	0.42
MEAM (4)	0.35	0.35	0.39	0.24
SNAP (4)	0.27	0.41	0.29	0.30
TabGAP (4)	0.17	0.45	0.22	0.20
MTP (4)	0.22	4.65	0.47	0.20
MACE-MP-0b3 (6)	0.27	0.32	0.09	0.23
MACE-MPA-0 (6)	0.18	0.22	0.10	0.07
MACE-MATPES (6)	0.16	0.20	0.15	0.14
NEP-2024 (5)	0.14	0.16	0.18	0.18
NEP89 (6)	0.21	0.23	0.25	0.17
UMA-S-1 (6)	0.10	0.10	1.76	0.07
GRACE-2L (6)	0.12	0.22	0.10	0.06

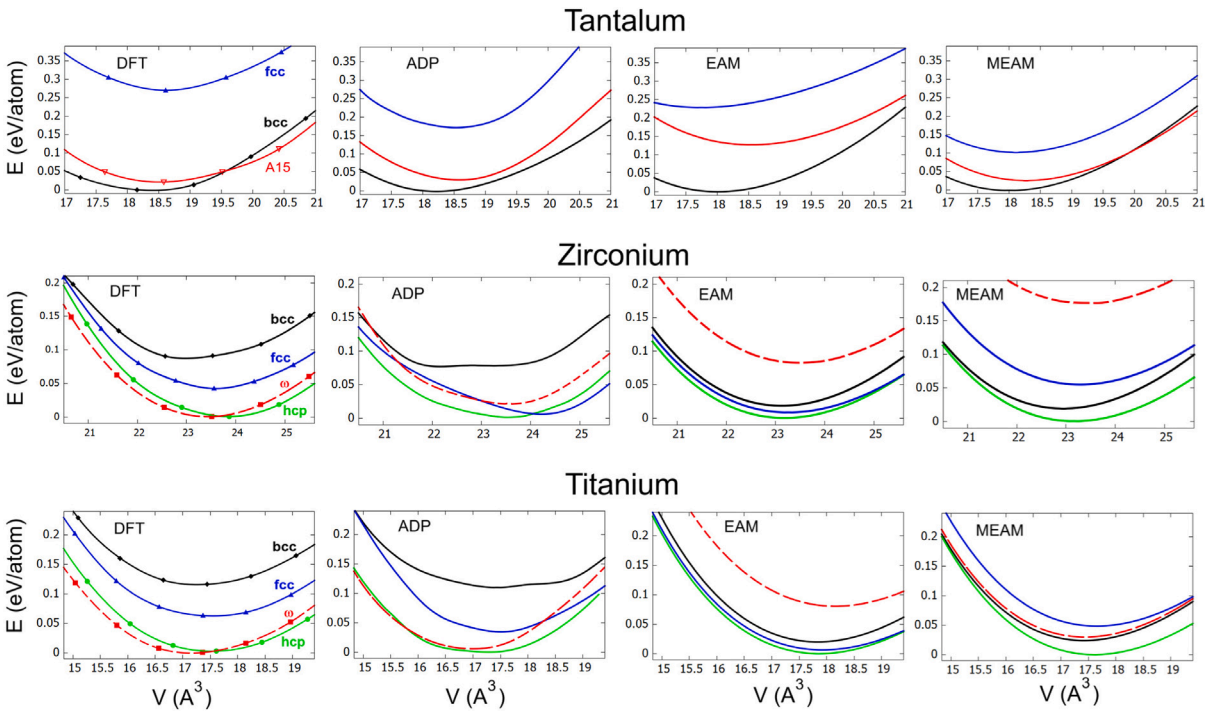

Fig. 1. Calculated energy–volume curves for the bcc, fcc, A15, hcp and ω phases of the simulated metals in comparison with DFT data [47,48]. The explanation of the curves is given for the DFT data panel.

displacement r, normalized by the equilibrium interatomic distance ρ_0. Calculations were performed for three modes – mode 1, mode 5, and mode 8 – using the notation introduced in the original work [50]. Fig. 2 presents these dependencies obtained with the ADP potential for W (along with published DFT data) and for Ta. The energy hierarchy of the modes is the same for both metals and is consistent with the DFT results.

Table 2 presented the basic properties of pure Ta calculated with the classical potentials compared to available DFT [51,52] and experimental data [53–55]. With static calculations, we have evaluated the lattice parameter a, elastic moduli C_{ij}, the formation and migration energies of the vacancy (E^f_{vac} and E^m_{vac}), and the formation energy of a self-interstitial atom E^f_{SIA} in the ground energy state. In addition, from the molecular dynamics simulation, we calculated the linear thermal expansion α_L and the melting temperature T_m using the two-phase simulation method [56,57]. The largest deviation from the reference data occurred with MEAM, which substantially underestimated the values of E^m_{vac} and T_m.

As a next step, we have calculated the relaxed generalized stacking fault energy (GSFE) profiles of pure Ta for the {110} and {112} slip planes when subjected to a displacement in the ⟨111⟩-direction. In Fig. 3, the results are compiled for the ADP, EAM and MEAM potentials along with DFT data. It is found that all empirical potentials produce unstable GSFE data in good agreement results from DFT, which predict that the energy barrier of the {110} slip plane is less than that of {112}. The largest deviation from DFT – in terms unstable stacking fault energies – occurs for the {112} slip plane for the ADP potential (overestimated by approx. 14%). However, it is only the ADP potential that gives rise to an asymmetric profile for the {112} plane, as predicted by DFT. The remaining potentials yield symmetric profiles with maxima halfway along the path, i.e. for displacement corresponding to $a\sqrt{3}/4$.

In Fig. 4, we have evaluated the ground state energy for a set of [110] symmetric tilt grain boundaries (GBs) with tilt angles in the range $11° < \theta < 169°$ as predicted by the ADP. This investigation was conducted as detailed in [58]. Comparison with available DFT data [59,60] reveals that the overall trend is captured. For instance, the low energy of the $\Sigma 3$ twin boundary matches that of 0.29 J/m^2 as found by means of DFT modeling [59]. Likewise, as representative among the high energy symmetric tilt GBs, the computed energy of the

Table 2
The tested properties of Ta: the simulated results for three classical potentials are compared with measured values [53–55] and DFT data [51,52].

	Expt.	DFT	EAM	MEAM	ADP
a (Å)	3.304	3.320	3.303	3.303	3.315
C_{11} (GPa)	266	266	262	266	265
C_{12} (GPa)	158	161	157	158	187
C_{44} (GPa)	86	76	82	87	99
E^f_{vac} (eV)	—	2.86	2.98	2.94	3.03
E^m_{vac} (eV)	—	0.76	0.99	0.34	0.98
E^f_{SIA} (eV)	—	4.77	4.95	4.86	5.94
T_m (K)	3293	—	3450	2570	2780
α_L (10^{-6} K^{-1})	7.4	—	5.2	6.4	7.1

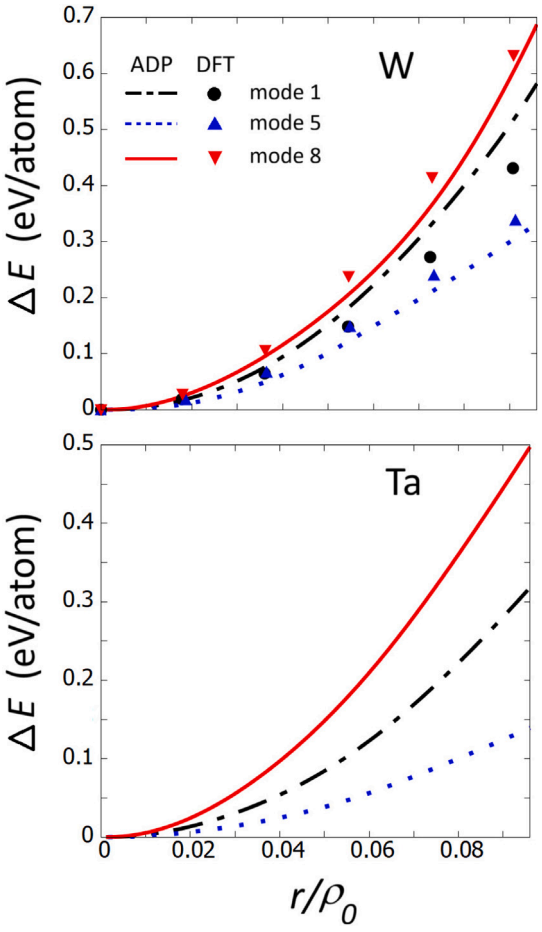

Fig. 2. Calculated dependence of the atomic energy on the DNVMs displacement normalized by the interatomic distance. (Upper panel) Results for W obtained using the ADP potential are compared with DFT data [50]. (Lower panel) Results for Ta calculated using the ADP potential.

$\Sigma 9$ GB with a tilt angle of θ =141° falls within the reported range of 1.5–1.6 J/m^2 [59,60]. These results confirm that the ADP has the capability to accurately predict the GB properties of pristine Ta.

To investigate the ADP's capability to describe low-coordinated configurations, we have evaluated the ground state energy of a set of Ta low-energy surfaces: (100), (110), (111) and (112). It is found that the ADP, along with EAM and MEAM, all predict the (110) to have the lowest surface energy, in accordance with results from DFT, see Fig. 5. Although the absolute energies are overestimated by the ADP potential by about 0.5 J/m^2, it does capture the relative energy hierarchy and the energy differences quite well.

A notable strength of the developed ADP potential is its ability to accurately reproduce the compact screw dislocation core in Ta, as it does for W, Nb, and Mo [26]. An accurate description of the dislocation core is essential to reliably simulate a wide range of dislocation-related phenomena, including plasticity, solute segregation, and pipe diffusion. Fig. 6 shows the relaxed core structure of the $1/2\langle 111\rangle$ screw dislocation in tantalum (displacement map) for all three classical potentials calculated using cylindrical cells constructed with `matscipy.dislocation` package [61]. The MEAM potential fails to reproduce the correct non-polarized dislocation core. For the ADP, the calculated magnitude of the glide barrier (Peierls barrier) for screw dislocations is 46 meV/b, where b is the Burgers vector. This value is close to the DFT estimate ~40 meV/b [62]. However, similar to many other classical potentials, the ADP potential predicts Peierls barriers with a "doubly-humped" profile, with a local minimum at the split-core state, which differs from DFT.

Atomistic simulation of hcp metals such as Ti and Zr is generally more difficult than for bcc metals like Ta or Mo. At room temperature, these metals have a highly anisotropic hexagonal close-packed (hcp) structure with multiple competing slip systems, including basal, prismatic, and pyramidal. Moreover, depending on temperature and stress, they can assume the shape of multiple crystal phases (e.g., hcp α-phase, bcc β-phase, and hexagonal ω-phase), each exhibiting distinct defect properties. Table 3 shows the basic properties of α-Zr and α-Ti calculated at zero temperature with use of the ADP potential. For this validation, we also calculated the energy of the $\Sigma 7$ twist type GB and compared it with results from our DFT calculations. The overall observation is that the ADP describes the energies of point and planar defects in both hcp metals with good accuracy.

To assess the ADP's ability to predict the stacking fault energetics for α-Zr and α-Ti, we evaluate the GSFE curves for slip on the basal and prismatic planes, see Fig. 7. For the basal plane we consider slip along the $[1\bar{1}00]$ and $[\bar{1}2\bar{1}0]$-directions. For the former slip system, it is found that the ADP underestimates stable stacking fault energy of Zr. It amounts to only 0.05 J/m^2, while the DFT data corresponds 0.24 J/m^2. This minuscule stacking fault energy is a mere reflection of the small energy difference between hcp and fcc Zr, as observed in Fig. 1. For basal slip in the $[\bar{1}2\bar{1}0]$-direction, although the unstable stacking fault energy is underestimated, it is seen that the overall characteristics of the DFT curve – with a single maximum – is reproduced. For slip on the prismatic plane the ADP potential captures most features, including the a local minimum at the center of the displacement curve, which was also predicted by DFT. Comparison with the EAM and MEAM potentials reveals that the latter tends to overestimate the energy barriers, while the performance of the EAM is on par with the ADP. For α-Ti, the overall agreement with DFT results is better – both in terms of stable and unstable stacking fault energies. While the stacking fault of MEAM and ADP energy concurs with DFT data, it is severely underestimated by the EAM potential. Conversely, the energy thresholds predicted by MEAM systematically overestimate the DFT data. Thus, the ADP parametrization for α-Ti provides a well-balanced account of the GSFE characteristics.

Atomistic simulation of the thermal expansion in hcp metals with classical interatomic potentials is challenging because the hexagonal structure is highly anisotropic, with different lattice parameters along

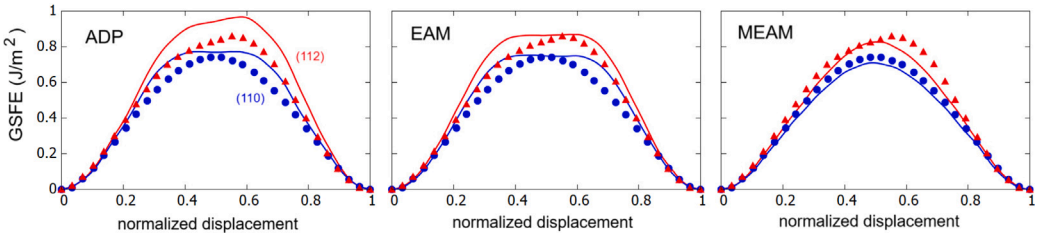

Fig. 3. GSFE curves for the [111]-direction in Ta, calculated with ADP, EAM, MEAM and DFT in this work. For normalized displacement along the pathway, a value of 1.0 corresponds to $a\sqrt{3}/2$.

Table 3
Basic properties of α-Zr and α-Ti at zero temperature: lattice parameters a (in Å) and c/a; elastic moduli C_{ij} (in GPa); vacancy formation energy E_v^f (in eV); SIA formation energy E_{sia}^f (in eV); GB energy E_{GB} for $\Sigma 7$ twist type (in J/m^2); surface energy E_s (in J/m^2). The results are compared with the available experimental data and DFT calculations.

	Expt. (Zr)	DFT (Zr)	ADP (Zr)	Expt. (Ti)	DFT (Ti)	ADP (Ti)
a	3.231 [63]	3.236 [64]	3.258	2.94 [65]	2.94 [66]	2.93
c/a	1.59 [63]	1.60 [64]	1.58	1.58 [65]	1.583 [66]	1.57
C_{11}	143 [67]	147 [64]	185	176 [68]	172 [66]	180
C_{12}	73 [67]	69 [64]	119	87 [68]	86 [66]	109
C_{13}	65 [67]	71 [64]	89	68 [68]	74 [66]	62
C_{33}	165 [67]	163 [64]	211	191 [68]	189 [66]	157
C_{44}	32 [67]	26 [64]	41	51 [68]	43 [66]	51
E_v^f	—	2.07 [69]	2.39	—	2.03 [70]	1.84
E_{sia}^f	—	2.73 [71]	3.04	—	2.58 [70]	2.52
E_{GB}	—	0.29	0.28	—	0.33	0.40
$E_s(0001)$	2.05 [72]	1.60 [73]	1.48	—	1.97 [74]	1.80
$E_s(10\bar{1}0)$	—	1.66 [73]	1.66	—	2.04 [74]	1.91

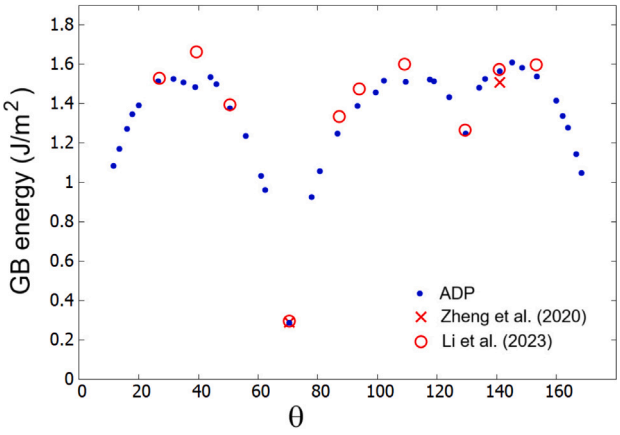

Fig. 4. GB energies for [110] symmetric tilt GBs in Ta, calculated for different tilt angles: ADP results are compared with DFT data [59,60].

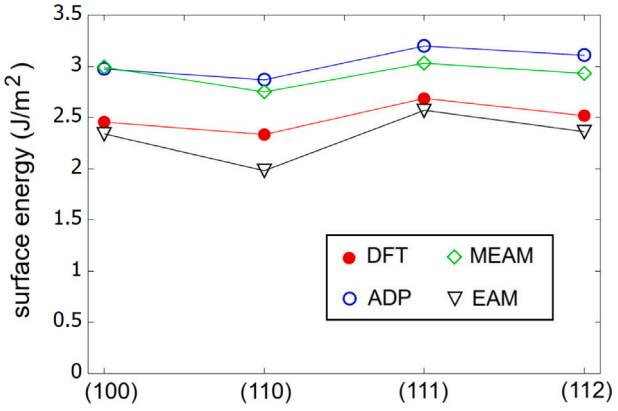

Fig. 5. Surface energies calculated for four different low-index surfaces of bcc Ta. ADP, EAM and MEAM results are compared with DFT predictions.

the a- and c-axes, leading to direction-dependent expansion. Classical potentials often fall short on capturing this anisotropy accurately and oversimplify anharmonic atomic vibrations [66,75]. In particular, classical potentials often struggle to reproduce the correct thermal dependence of c/a ratio, which is essential for accurately simulating phase stability and defect-mediated properties. Fig. 8 illustrates the calculated thermal expansion for all three classical potentials tested in this work. Additionally, the figure includes the experimentally measured dependencies for validation. It is found that the ADP accurately reproduces the temperature dependence of the c/a ratio for both Zr and Ti.

The ability to capture the thermally-induced transition to the bcc phase is a key requirement for interatomic potentials of Ti and Zr. Other studies have shown that the EAM and MEAM potentials used here are unable to predict this transition [78,79]. Unlike these models, the new ADP predicts the hcp–bcc phase transformation at temperatures close to the experimental values, see Table 4. In the spirit of the previous work [36], we have estimated the transition temperature $T_{\alpha\beta}$ from the intersection of the temperature stability ranges of the α and β phases. Specifically, in simulations at $T = 800$ K, β-Ti remains stable for only a few picoseconds before spontaneously transforming back into α-Ti. In contrast, α-Ti remains stable up to about 1630 K, above which it transforms into the bcc structure. Thus, the transition temperature can be estimated as $T_{\alpha\beta} \approx 1250$ K. Table 4 contains the key characteristics of α-β transition and melting calculated with ADP together with the measured values [80–87].

5. Properties of binary alloys

This section is devoted to the discussion of properties of binary systems that can be simulated using the new potential. It should be noted that the validation of the W–Mo–Nb part has already been carried out in several previous works [24–26], and thus we focus only on other systems here.

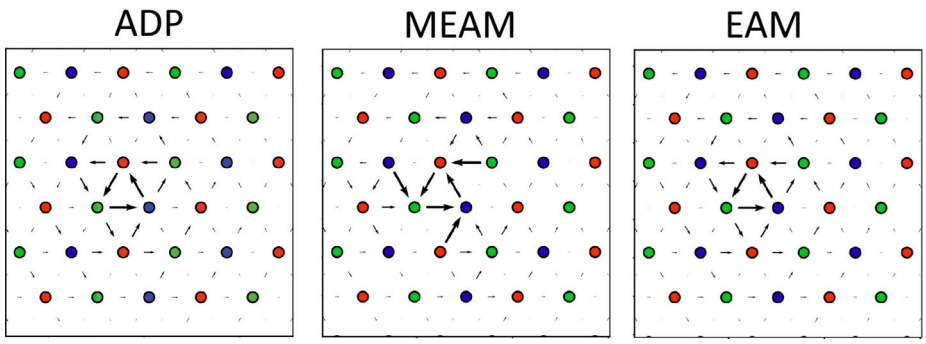

Fig. 6. Structure of the screw dislocation core in Ta described by the classical potentials.

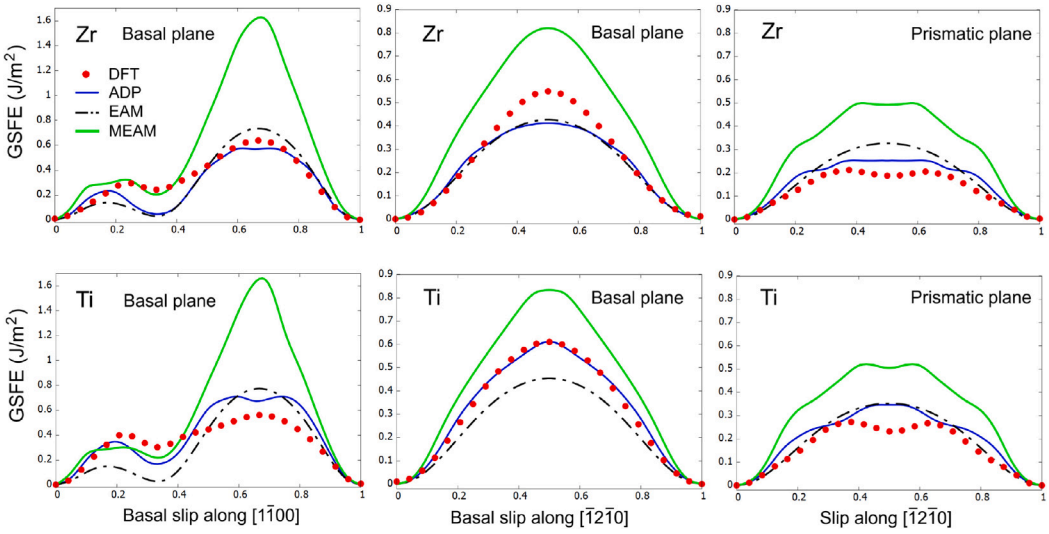

Fig. 7. GSFE curves for Zr and Ti, calculated with ADP, EAM, MEAM and DFT in this work.

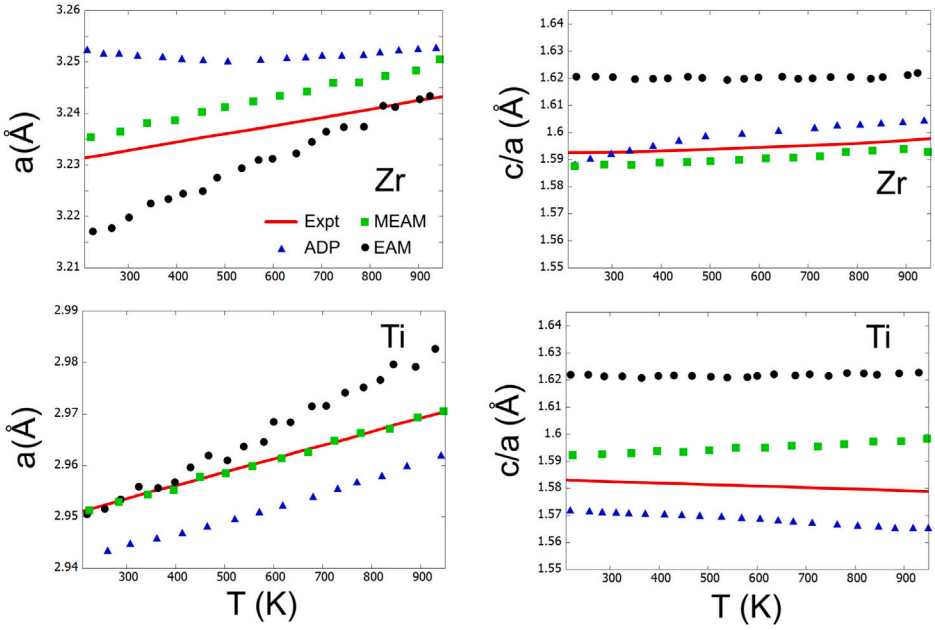

Fig. 8. Thermal dependence of a and c/a in Zr and Ti simulated by classical potentials at comparison with the experimental data [65,76,77].

Table 4
Characteristics of phase transitions and basic properties of β-Zr and β-Ti. The table contains transition temperature $T_{\alpha\beta}$ (in K); transition enthalpy $H_{\alpha\beta}$ (in eV/atom); volume change $\Delta V_{\alpha\beta}$ (in %); melting temperature T_m (in K); melting enthalpy H_m (in eV/atom). The properties of β-phase at $T = 1200$ K include a (in Å) and thermal expansion α_V (in 10^{-5} K^{-1}).

	Expt. (Zr)	ADP (Zr)	Expt. (Ti)	ADP (Ti)
$T_{\alpha\beta}$	1130 [83]	1310 ± 50	1155 [80]	1250 ± 50
$H_{\alpha\beta}$	0.042 [84]	0.041	0.044 [80]	0.046
$\Delta V_{\alpha\beta}$	−0.45 [85]	0.67	−0.05 [85]	0.2
T_m	2130 [86]	1860 ± 50	1941 [80]	1720 ± 50
H_m	0.184 [82,87]	0.137	0.157 [80]	0.105
a	3.62 [81,85]	3.64	3.31 [85]	3.28
α_V	2.9 [81,85]	1.47	4.1 [85]	1.05

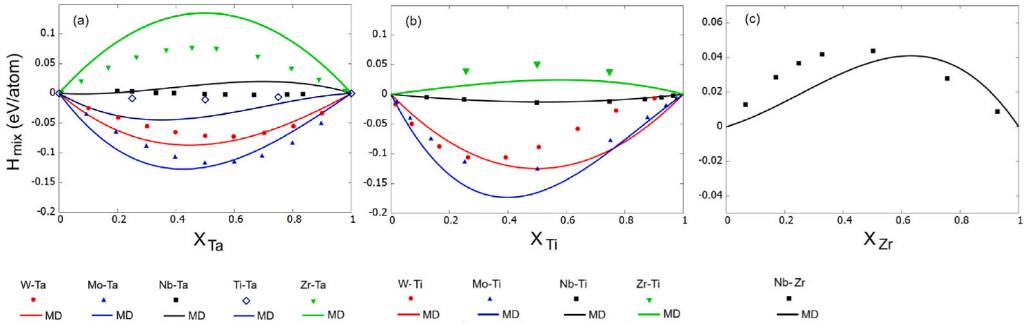

Fig. 9. The mixing enthalpy of bcc random solution for (a) Ta-based alloys, (b) Ti-based alloys and (c) Nb–Zr alloy. In all panels, the lines correspond to the MD calculations with ADP at $T = 0$ K for W–Ta, Mo–Ta, Nb–Ta and Zr–Ti (hcp alloy) and at $T = 1250$ K for other alloys; symbols represent the thermodynamic estimation based on experimental data [88,89] or DFT calculations [16,90–93].

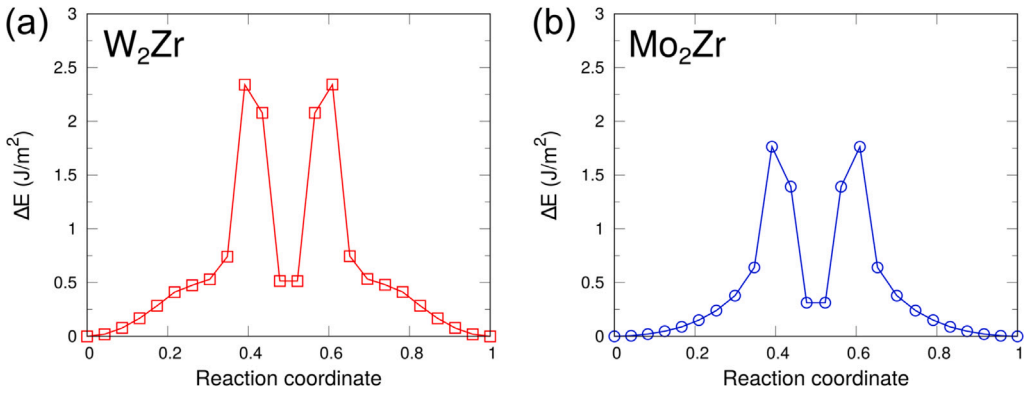

Fig. 10. Minimal energy path for the {111}⟨110⟩ slip via the synchroshear slip mechanism calculated using nudged elastic band with the ADP potential: (a) W_2Zr and (b) Mo_2Zr C15 Laves phases.

5.1. Mixing enthalpy

Reliable mixing enthalpy of random alloys is essential for predicting phase diagrams, solubility limits, and miscibility gaps. These govern whether alloys will form solid solutions, ordered phases, or phase-separates. Thus, to validate the ability of the ADP to predict a realistic thermodynamic description, we computed the mixing enthalpy H_{mix} at zero temperature and pressure for three binary random bcc alloys (W–Ta, Mo–Ta, Nb–Ta) and one hcp alloy (Ti–Zr). Also, we calculated H_{mix} for several bcc-phase alloys with varying composition at $T = 1250$ K: Ti–Ta, Zr–Ta, W–Ti, Mo–Ti, Nb–Ti and Nb–Zr. Fig. 9 shows the calculated dependence of H_{mix} on the alloy composition together with the thermodynamic estimates based on experimental data [88,89] or DFT calculations [16,90–93]. According to the calculation results, ADP reproduces the energy hierarchy of alloys and can therefore be used to study the order–disorder transition in CCRAs. Fig. 9 does not report H_{mix} for Mo–Zr and W–Zr binary alloys, since they become structurally distorted at compositions near the stable compounds Mo_2Zr and W_2Zr that exist in these alloys [94–96].

5.2. W_2Zr and Mo_2Zr laves phases

To accurately describe the W_2Zr and Mo_2Zr Laves phases is essential for atomistic simulation of CCRAs, as these intermetallic compounds play a key role in determining the thermodynamic stability, microstructural evolution, and mechanical properties of the alloys. Laves phases are among the most stable compounds in Mo–Zr and W–Zr subsystems, and their formation strongly affects phase equilibria, solute segregation, and defect properties [99]. Since they often precipitate as hard, brittle phases, their energetics and stability directly influence the alloy strength, creep resistance, and high-temperature performance.

Laves phases can exist in three different polymorphic structures: hexagonal types C14 and, as well as the cubic type C15. According to measurements [94–96], W_2Zr and Mo_2Zr have structure of the C15-Laves phase. The ADP accurately predicts that type C15 to be the most stable compound for both alloys, see Table 5, which presents the formation enthalpies and lattice parameters of the C14, C15, and C36 compounds as predicted by the ADP potential. For validation, the

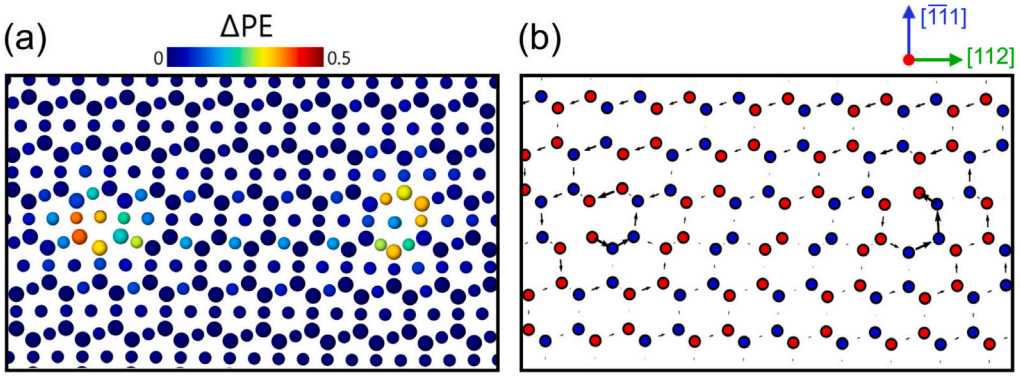

Fig. 11. Dissociation of a full $\frac{1}{2}[\bar{1}10]$ screw dislocation into two 30° synchro-Shockley partial dislocations on the $(\bar{1}\bar{1}0)$ plane bounded by a stacking fault in the C15 Mo_2Zr Laves phase using the ADP potential: (a) Dislocation core structure, color-coded by excess potential energy (in eV), where large particles denote Zr atoms and small particles denote Mo atoms. (b) Differential displacement map of the Zr sublattice, with atoms color-coded by atomic layers along the $[\bar{1}10]$ direction.

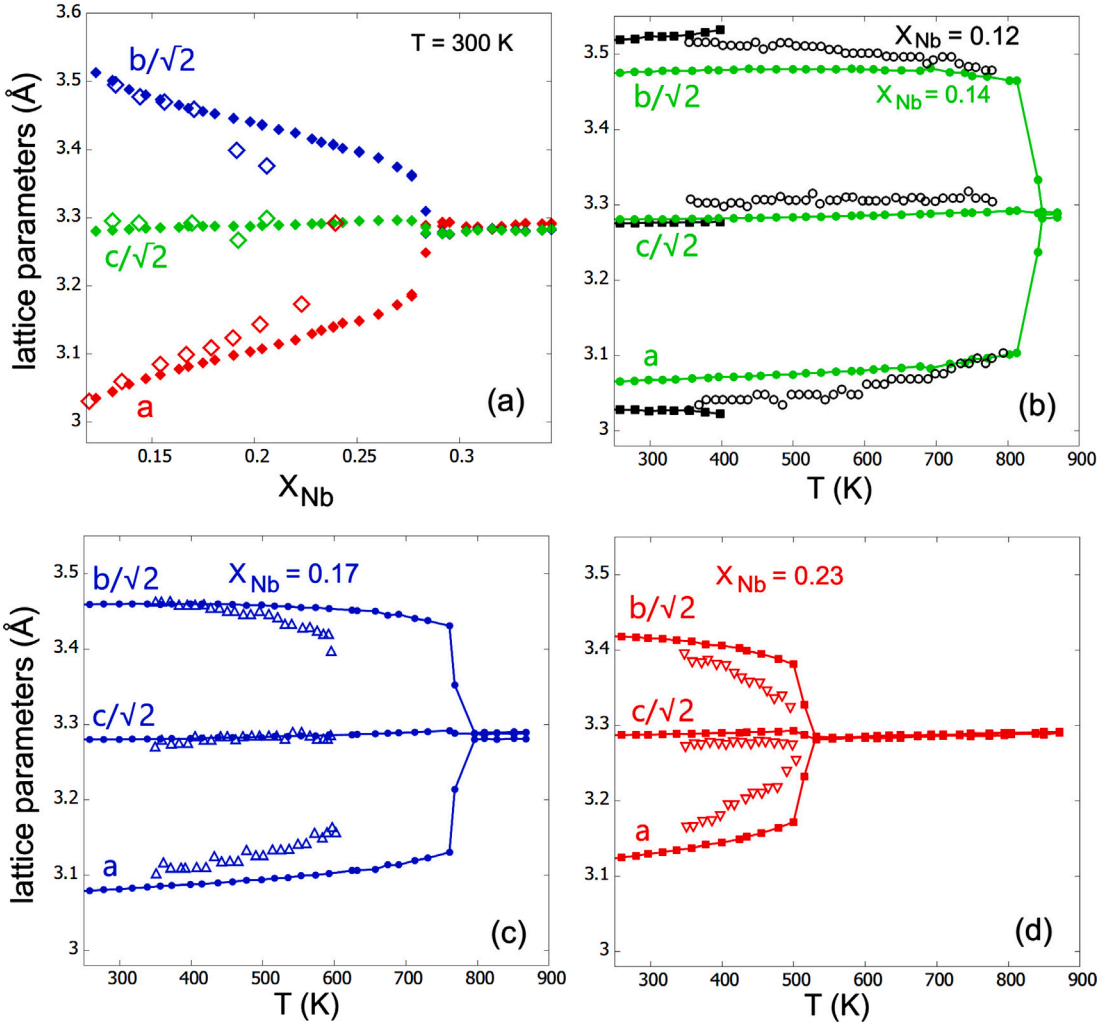

Fig. 12. Lattice parameters of α'' Ti–Nb alloy calculated using ADP (filled symbols with lines) and measured in experiments [97,98] (empty symbols). (a) Dependence of parameters on composition at room temperature. High Nb content (or high temperature) leads to transition to the bcc lattice. (b)–(d) The temperature dependence of the lattice parameters for various alloys. For panel (b) the simulation results are given for alloys with 12at.% (black) and 14at.% (green) niobium.

table also includes DFT data obtained from the OQMD database [100,101]. According to the simulation results, ADP correctly reproduces the energy hierarchy of these phases for both the Mo_2Zr and W_2Zr compounds.

To validate the description of the C15 Laves phase, we calculated the elastic moduli, volumetric thermal expansion α_V, melting temperature and formation energies of point defects. In this work, we considered only the reaction energies of point defects in A_2B

Table 5
Characteristics of Laves phases in W-Zr and Mo-Zr binary systems. The table contains formation enthalpies (in eV/atom) and lattice parameters (in Å) for C14, C15 and C36 phases. DFT data for comparison were taken from the OQMD database [100,101].

	W_2Zr		Mo_2Zr	
	DFT	ADP	DFT	ADP
H_{C14}	−0.116	−0.110	−0.114	−0.137
H_{C15}	−0.144	−0.134	−0.138	−0.141
H_{C36}	−0.132	−0.124	−0.129	−0.138
a in C14	5.445	5.368	5.422	5.378
c in C14	8.765	8.846	8.683	8.737
a in C15	7.656	7.639	7.615	7.609
a in C36	5.423	5.399	5.394	5.380
c in C36	17.605	17.627	17.484	17.527

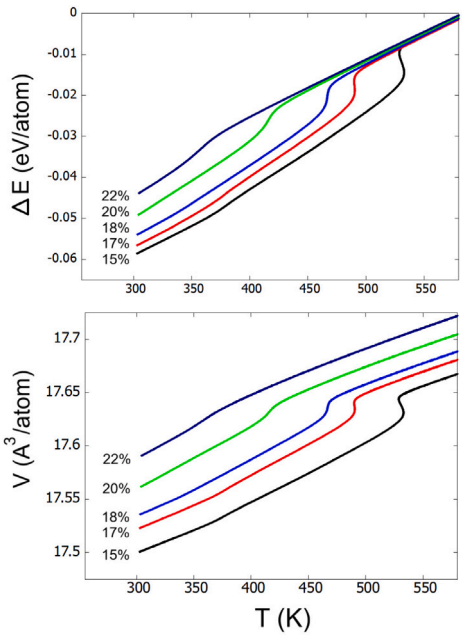

Fig. 13. Change in potential energy and atomic volume during cooling of Ti–Nb alloys. Atomic percentages of niobium are shown near the calculated curves.

compounds that can be evaluated without invoking the concept of chemical potential [102–104]. Specifically, we calculated the formation energies of the following complex defects: the Schottky trio (E_{ST}), the antisite pair (E_{AsP}), the A-type Frenkel pair (E_{AFP}), and the B-type Frenkel pair (E_{BFP}), where A represents Mo or W and B corresponds to Zr. The results for ADP and DFT calculations are presented in Table 6. It can be observed that, due to the low values of E_{AsP}, temperature-induced disordering is primarily associated with the accumulation of antisite defects, which is typically the case in Laves phases [105].

Synchroshear is widely recognized as the most energetically favorable slip mechanism on {111} planes in C15 Laves phases, especially at the elevated temperatures [106,107]. We calculated the minimal energy path for {111}⟨110⟩ slip in C15 W_2Zr and Mo_2Zr Laves phases using the nudged elastic band method [108,109] with the ADP potential. As illustrated in Fig. 10, the ADP potential successfully predicts the synchoshear mechanisms as the most favorable pathway in both C15 Laves phases, namely, the energy profile features two identical peaks corresponding to the leading and trailing synchro-Shockley partial slip events, separated by a metastable stacking fault state. The stacking fault structures were further relaxed, and the stable stacking fault energies of C15 W_2Zr and Mo_2Zr Laves phases were found to be 160 mJ/m^2 and 32 mJ/m^2, respectively.

Table 6
Characteristics of C15 structure for W_2Zr and Mo_2Zr compounds. The table contains elastic moduli C_{ij} (in GPa), formation energy of point defects (in eV), thermal expansion α_V (in 10^{-5} K^{-1}) and melting temperature T_m (in K). The predictions of ADP potential were compared with DFT data calculated in this work.

	DFT (W_2Zr)	ADP (W_2Zr)	DFT (Mo_2Zr)	ADP (Mo_2Zr)
C_{11}	314	352	257	389
C_{12}	163	195	155	250
C_{44}	95	155	64	84
E_{ST}	12.6	11.28	10.9	9.27
E_{AFP}	9.98	9.31	8.8	7.43
E_{BFP}	11.95	11.02	11.2	8.25
E_{AsP}	2.71	2.38	2.25	2.33
α_V	–	0.6	–	2.7
T_m	–	2910	–	2480

The {111}⟨110⟩ dislocation structures and energies in the C15 Mo_2Zr Laves phase were further evaluated using the ADP potential. Fig. 11 shows the dissociation of a full $\frac{1}{2}[\bar{1}10]$ screw dislocation in the C15 Mo_2Zr Laves phase, simulated using the ADP potential. The details of dislocation insertion and simulation setup are provided in [110]. The dislocation splits into two 30° synchro-Shockley partials on the $(\bar{1}\bar{1}0)$ plane, separated by a stacking fault ribbon. In the excess potential energy map (Fig. 11(a)), localized regions of elevated energy mark the positions of the partial dislocations, while the stacking fault region, especially the Mo sublattice, exhibits a uniform excess energy. Notably, the ADP potential successfully captures the presence of two distinct types of 30° synchro-Shockley partials with different core structures (see Fig. 11(a) and (b)), which arise from the low crystalline symmetry of Laves phases [110]. Furthermore, the predicted core configurations show good agreement with experimental observations from high-resolution scanning transmission electron microscopy [111,112] and with prior atomistic simulations of other Laves phases using MEAM potentials [107,110].

5.3. Phase transitions in Ti–Nb alloy

Titanium-based alloys stand out among CCRAs because they are capable of exhibiting shape memory effect (SME) and superelasticity (SE) [113–115]. Both phenomena take place due to a reversible martensitic phase transformation when a bcc β-phase transforms into an orthorhombic α''-martensite phase upon loading or temperature variation. To find out how ADP describes this transformation, we performed several simulations for Ti–Nb alloys.

The α''-phase is defined by three parameters: a, b, and c. We calculated the dependence of these parameters on temperature and composition in the Ti–Nb system. An increase in temperature or Nb content leads to a transformation into a bcc lattice via the Burgers mechanism. The modeling with NPT-equilibration was carried out using a relatively small system of 4000 atoms. The simulation results presented in Fig. 12 confirm that the ADP accurately reproduces the experimentally observed changes in the α'' lattice [97,98] with varying temperature or Nb content. Only when the Nb concentration is below 13 at.%, heating of the α''-phase results in the transformation into an ω-like structure.

As a final step in this validation, we performed large-scale atomistic simulations illustrating the transformation that occurs in the β-alloy upon cooling. The simulated system consisted of $3.2{\cdot}10^7$ atoms and was cooled at a rate of 1 K/ps under zero-pressure condition. Although this cooling rate is considerably higher than those typically achievable in experiments, such rates are common in molecular dynamics simulations due to time-scale limitations. Periodic boundary conditions were applied for all directions. The initially created bcc alloy was transformed into α''-martensitic structure at a temperature close to the transition temperature (slight supercooling can be realized with this

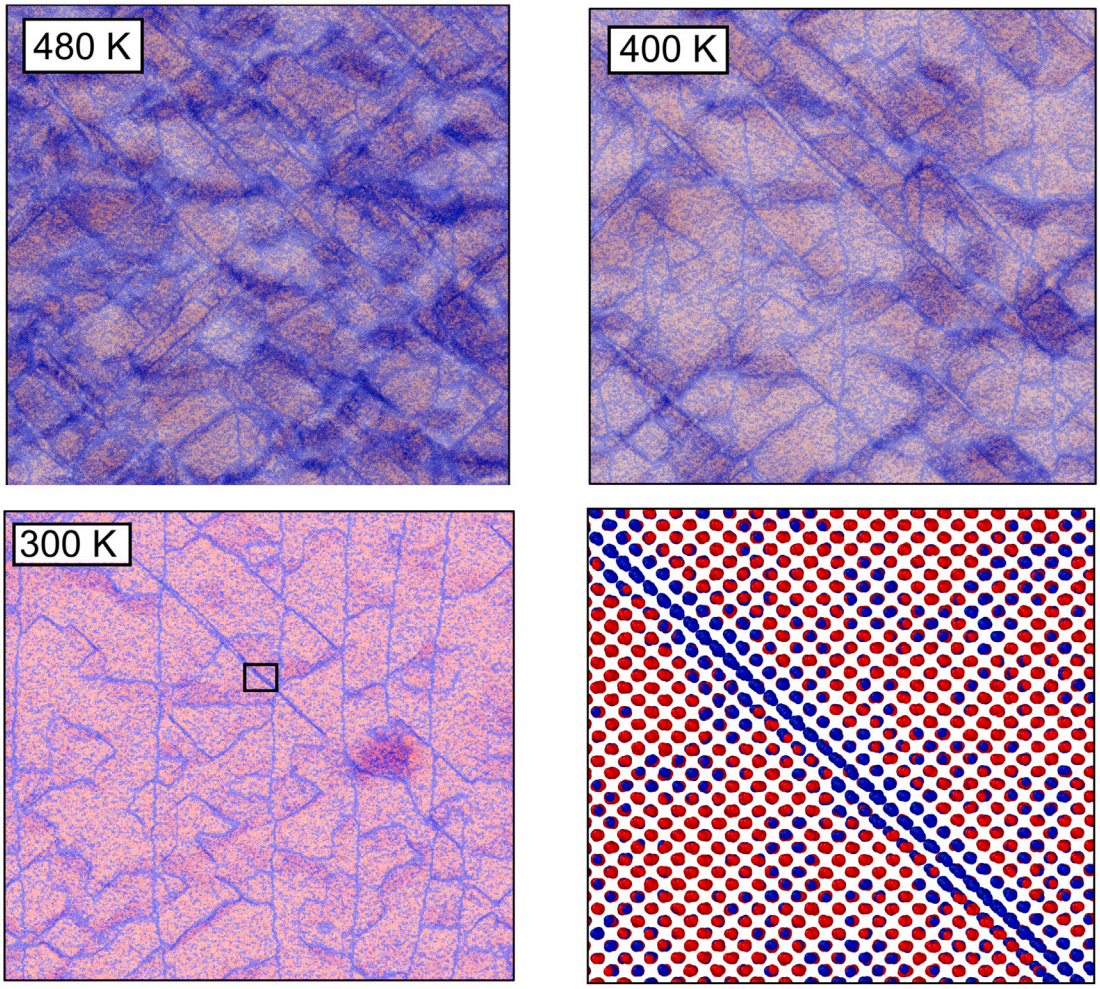

Fig. 14. Snapshots of the large-scale MD simulation of Ti–17Nb alloy at the cooling. Three snapshots correspond to different temperatures, and one image shows a magnified view of the atomic structure in the final state (black box in the snapshot at $T = 300$ K). The color of the atoms is related to the analysis based on local elastic strain: red atoms and blue atoms belong to the α'' martensite structure and crystal defects, respectively.

type of modeling). Since the martensitic transformation occurs locally and without atomic diffusion, the simulation results can be regarded as qualitatively reliable. Fig. 13 shows the temperature dependence of volume and energy (relative to the β-lattice) in the simulation. It can be seen that for Nb contents above 18 at.%, the transition begins to exhibit characteristics of a reversible transformation, as the changes in volume and energy become smoother. This observation is consistent with experimental findings that the SME and SE phenomena occur in Ti–Nb alloys with Nb content ranging from 19 at.% to 27 at.% [114].

It is interesting to discuss here the textural structure of the α''-phase formed during large-scale simulations. Since the transformation occurs via the Burgers mechanism without shear distortions, the resulting alloy did not contain mainly common GBs, but consisted of various partially coherent variants of α''-lattice. The snapshots illustrating the gradual formation of such texture are given in Fig. 14. The α''-phase variants are separated by twinning interfaces, and the average size of a variant in such structure is about 25 nm. A detailed study of this self-accommodation morphology of martensite will be the subject of future research.

6. Conclusion

This work describes the development and validation of a new interatomic potential for refractory alloys based on the W–Mo–Nb–Ta–Zr–Ti system. The main objective of this work was to create a classical potential that could simulate large-scale atomic systems, as previous universal machine learning (ML) models were computationally too expensive for simulations with over 10^4 atoms. The developed ADP model was comprehensively validated against DFT data and other interatomic potentials, demonstrating its ability to accurately reproduce various properties and behaviors of the alloys, including structural transformations and crystal defects. Although the ADP force error was found to be higher than that of ML models, its significant computational efficiency – approximately 1000 times lower cost – makes it a valuable tool for large-scale atomistic simulations. The study highlights the ADP accuracy in describing key properties of pure metals like Ti and Ta, and its capability to predict crucial phenomena such as the hcp–bcc phase transformation of Ti and Zr, which other classical potentials fail to capture. The potential also successfully reproduces the energy hierarchy of binary alloys, accurately predicts the stability of Laves phases, and models the martensitic phase transformation in Ti–Nb alloys.

CRediT authorship contribution statement

Sergei Starikov: Writing – original draft, Supervision, Project administration, Investigation, Conceptualization. **Petr Grigorev:** Writing – review & editing, Investigation. **Sang-Hyeok Lee:** Investigation. **Zhuocheng Xie:** Writing – review & editing, Methodology, Investigation. **Pär A.T. Olsson:** Writing – review & editing, Methodology, Investigation.

Declaration of competing interest

The authors declare the following financial interests/personal relationships which may be considered as potential competing interests: Sergei Starikov reports financial support was provided by German Research Foundation. Pär Olsson reports financial support was provided by Swedish Research Council. Sang-Hyeok Lee reports financial support was provided by German Research Foundation. Zhuocheng Xie reports financial support was provided by German Research Foundation. If there are other authors, they declare that they have no known competing financial interests or personal relationships that could have appeared to influence the work reported in this paper.

Acknowledgments

The authors thank Prof. M. Bönisch and Dr. S. Dubinskiy for their valuable discussions on the properties of Ti alloys. Sergei Starikov gratefully acknowledges the financial support from the German Research Foundation, project 548597133. Pär Olsson gratefully acknowledges the financial support from the Swedish Research Council, project 2022-04497. Sang-Hyeok Lee and Zhuocheng Xie acknowledge financial support funded by the Deutsche Forschungsgemeinschaft (DFG) in the SFB1394 “Structural and chemical atomic complexity – from defect phase diagrams to material properties” (Project ID 409476157). Zhuocheng Xie acknowledges financial support funded by the DFG – Projektnummer 562592407. The calculations were carried out on the computer clusters Vulcan (ICAMS Computing cluster, RUB), Noctua2 (Paderborn Center for Parallel Computing, Project “Direfra”), and Tetralith (National Supercomputer Centre, Linköping University, via allocations provided by the National Academic Infrastructure for Supercomputing in Sweden (NAISS)). Petr Grigorev used access to the HPC resources of IDRIS under the allocation R1001010339R1 attributed by GENCI. Sang-Hyeok Lee and Zhuocheng Xie gratefully acknowledge the computing time provided to them at the NHR Center NHR4CES at RWTH Aachen University (project numbers p0021574).

Appendix A. Supplementary data

Supplementary material related to this article can be found online at https://doi.org/10.1016/j.commatsci.2025.114369.

Data availability

Data will be made available on request.

References

[1] T. Zhang, H. Deng, Z. Xie, R. Liu, J. Yang, C. Liu, X. Wang, Q. Fang, Y. Xiong, Recent progresses on designing and manufacturing of bulk refractory alloys with high performances based on controlling interfaces, J. Mater. Sci. Technol. 52 (2020) 29–62.

[2] C.V. Funch, G. Proust, Laser-based additive manufacturing of refractory metals and their alloys: A review, Addit. Manuf. 94 (2024) 104464.

[3] A. Pramanik, C. Konkati, S. Laube, L. Yang, S. Sen, A. Kauffmann, M. Heilmaier, A. Chauhan, Exploring room-temperature deformation mechanisms of a b2-strengthened refractory compositionally complex alloy, Mater. Sci. Eng.: A 931 (2025) 148180.

[4] O. Senkov, G. Wilks, D. Miracle, C. Chuang, P. Liaw, Refractory high-entropy alloys, Intermetallics 18 (2010) 1758–1765.

[5] O.N. Senkov, G.B. Wilks, J.M. Scott, D.B. Miracle, Mechanical properties of nb25mo25ta25w25 and v20nb20mo20ta20w20 refractory high entropy alloys, Intermetallics 19 (2011) 698–706.

[6] O.N. Senkov, D.B. Miracle, K.J. Chaput, J.-P. Couzinie, Development and exploration of refractory high entropy alloys—a review, J. Mater. Res. 33 (2018) 3092–3128.

[7] H. Yao, J. Qiao, J. Hawk, H. Zhou, M. Chen, M. Gao, Mechanical properties of refractory high-entropy alloys: Experiments and modeling, J. Alloys Compd. 696 (2017) 1139–1150.

[8] A. Vyazmin, A. Lipnitskii, A. Kartamyshev, V. Maksimenko, D. Poletaev, N-body potential for simulation of α and β phases of zirconium, Comput. Mater. Sci. 235 (2024) 112806.

[9] S. Starikov, Y. Lysogorskiy, M. Qamar, A. Bochkarev, M. Mrovec, R. Drautz, Atomic cluster expansion for the aluminum-magnesium-hydrogen system, Phys. Rev. Mater. 9 (2025) 103606.

[10] K. Chen, C. Lin, H. Li, C. Hou, Y. Wu, L. Ma, J. Ye, J. Rong, X. Yu, Z. Liu, et al., Development of a deep potential model for fept alloys: Dft-level accuracy in high-temperature mechanical simulations, Mater. Today Commun. (2025) 113401.

[11] X.-G. Li, C. Chen, H. Zheng, Y. Zuo, S.P. Ong, Complex strengthening mechanisms in the nbmotaw multi-principal element alloy, Npj Comput. Mater. 6 (2020) 70.

[12] S. Yin, Y. Zuo, A. Abu-Odeh, H. Zheng, X.-G. Li, J. Ding, S.P. Ong, M. Asta, R.O. Ritchie, Atomistic simulations of dislocation mobility in refractory high-entropy alloys and the effect of chemical short-range order, Nat. Commun. 12 (2021) 4873.

[13] J. Byggmästar, K. Nordlund, F. Djurabekova, Modeling refractory high-entropy alloys with efficient machine-learned interatomic potentials: Defects and segregation, Phys. Rev. B 104 (2021) 104101.

[14] J. Byggmästar, K. Nordlund, F. Djurabekova, Simple machine-learned interatomic potentials for complex alloys, Phys. Rev. Mater. 6 (2022) 083801.

[15] V. Maksimenko, A. Lipnitskii, V. Saveliev, A. Kartamyshev, A. Vyazmin, D. Poletaev, N-body interatomic potential for molecular dynamics simulations of V-Cr-Nb-Mo-Ta-W system, Comput. Mater. Sci. 247 (2025) 113533.

[16] W.P. Huhn, M. Widom, Prediction of a2 to b2 phase transition in the high-entropy alloy mo-nb-ta-w, Jom 65 (2013) 1772–1779.

[17] P. Singh, A.V. Smirnov, D.D. Johnson, Ta-nb-mo-w refractory high-entropy alloys: anomalous ordering behavior and its intriguing electronic origin, Phys. Rev. Mater. 2 (2018) 055004.

[18] X.W. Zhou, R. Johnson, H.N. Wadley, Misfit-energy-increasing dislocations in vapor-deposited cofe/nife multilayers, Phys. Rev. B 69 (2004) 144113.

[19] M.S. Nitol, M.J. Echeverria, K. Dang, M.I. Baskes, S.J. Fensin, New modified embedded-atom method interatomic potential to understand deformation behavior in vnbtatizr refractory high entropy alloy, Comput. Mater. Sci. 237 (2024) 112886.

[20] H. Sharifi, C.D. Wick, Developing interatomic potentials for complex concentrated alloys of cu, ti, ni, cr, co, al, fe, and mn, Comput. Mater. Sci. 248 (2025) 113595.

[21] H. Yu, M. Giantomassi, G. Materzanini, J. Wang, G.-M. Rignanese, Systematic assessment of various universal machine-learning interatomic potentials, Mater. Genome Eng. Adv. 2 (2024) 58.

[22] B. Focassio, L.P.M. Freitas, G.R. Schleder, Performance assessment of universal machine learning interatomic potentials: Challenges and directions for materials’ surfaces, ACS Appl. Mater. & Interfaces 17 (2024) 13111–13121.

[23] Y. Lysogorskiy, A. Bochkarev, R. Drautz, Graph atomic cluster expansion for foundational machine learning interatomic potentials, 2025, arXiv preprint arXiv:2508.17936.

[24] S. Starikov, P. Grigorev, R. Drautz, S.V. Divinski, Large-scale atomistic simulation of diffusion in refractory metals and alloys, Phys. Rev. Mater. 8 (2024) 043603.

[25] S. Starikov, Dislocation mobility function as a key to understanding plasticity of refractory metals and alloys, Comput. Mater. Sci. 246 (2025) 113411.

[26] S. Starikov, P. Grigorev, P.A.T. Olsson, Angular-dependent interatomic potential for large-scale atomistic simulation of w-mo-nb ternary alloys, Comput. Mater. Sci. 233 (2024) 112734.

[27] See supplementary materials, 2026.

[28] Y. Mishin, M. Mehl, D. Papaconstantopoulos, Phase stability in the fe–ni system: Investigation by first-principles calculations and atomistic simulations, Acta Mater. 53 (2005) 4029–4041.

[29] S. Starikov, D. Smirnova, T. Pradhan, Y. Lysogorskiy, H. Chapman, M. Mrovec, R. Drautz, Angular-dependent interatomic potential for large-scale atomistic simulation of iron: Development and comprehensive comparison with existing interatomic models, Phys. Rev. Mater. 5 (2021) 063607.

[30] F. Ercolessi, J.B. Adams, Interatomic potentials from first-principles calculations: the force-matching method, Europhys. Lett. 26 (1994) 583.

[31] P. Brommer, F. Gähler, Potfit: effective potentials from ab initio data, Modelling Simul. Mater. Sci. Eng. 15 (2007) 295.

[32] P. Brommer, A. Kiselev, D. Schopf, P. Beck, J. Roth, H.-R. Trebin, Classical interaction potentials for diverse materials from ab initio data: a review of potfit, Modelling Simul. Mater. Sci. Eng. 23 (2015) 074002.

[33] S. Starikov, D. Smirnova, T. Pradhan, I. Gordeev, R. Drautz, M. Mrovec, Angular-dependent interatomic potential for large-scale atomistic simulation of the fe-cr-h ternary system, Phys. Rev. Mater. 6 (2022) 043604.

[34] S. Starikov, I. Gordeev, Y. Lysogorskiy, L. Kolotova, S. Makarov, Optimized interatomic potential for study of structure and phase transitions in si-au and si-al systems, Comput. Mater. Sci. 184 (2020) 109891.

[35] G. Kresse, J. Furthmüller, Efficient iterative schemes for ab initio total-energy calculations using a plane-wave basis set, Phys. Rev. B 54 (1996) 11169.

[36] S. Starikov, D. Smirnova, Optimized interatomic potential for atomistic simulation of zr-nb alloy, Comput. Mater. Sci. 197 (2021) 110581.

[37] S. Starikov, Dft dataset of w-nb-mo alloy calculations, 2024, http://dx.doi.org/10.17172/nomad/2024.05.16-1.

[38] S. Starikov, Dft dataset of w-nb-mo-ta-zr-ti calculations, 2025, http://dx.doi.org/10.17172/nomad/2025.10.03-1.

[39] C.A. Becker, F. Tavazza, Z.T. Trautt, R.A.B. De Macedo, Considerations for choosing and using force fields and interatomic potentials in materials science and engineering, Curr. Opin. Solid State Mater. Sci. 17 (2013) 277–283.

[40] L.M. Hale, Z.T. Trautt, C.A. Becker, Evaluating variability with atomistic simulations: the effect of potential and calculation methodology on the modeling of lattice and elastic constants, Modelling Simul. Mater. Sci. Eng. 26 (2018) 055003.

[41] K. Song, R. Zhao, J. Liu, Y. Wang, E. Lindgren, Y. Wang, S. Chen, K. Xu, T. Liang, P. Ying, et al., General-purpose machine-learned potential for 16 elemental metals and their alloys, Nat. Commun. 15 (2024) 10208.

[42] B. Deng, P. Zhong, K. Jun, J. Riebesell, K. Han, C.J. Bartel, G. Ceder, Chgnet as a pretrained universal neural network potential for charge-informed atomistic modelling, Nat. Mach. Intell. 5 (2023) 1031–1041.

[43] J. Schmidt, T.F. Cerqueira, A.H. Romero, A. Loew, F. Jäger, H.-C. Wang, S. Botti, M.A. Marques, Improving machine-learning models in materials science through large datasets, Mater. Today Phys. 48 (2024) 101560.

[44] I. Batatia, P. Benner, Y. Chiang, A.M. Elena, D.P. Kovács, J. Riebesell, X.R. Advincula, M. Asta, W.J. Baldwin, N. Bernstein, A. Bhowmik, S.M. Blau, V. Cărare, J.P. Darby, S. De, F.D. Pia, V.L. Deringer, R. Elijošius, Z. El-Machachi, E. Fako, A.C. Ferrari, A. Genreith-Schriever, J. George, R.E.A. Goodall, C.P. Grey, S. Han, W. Handley, H.H. Heenen, K. Hermansson, C. Holm, J. Jaafar, S. Hofmann, K.S. Jakob, H. Jung, V. Kapil, A.D. Kaplan, N. Karimitari, N. Kroupa, J. Kullgren, M.C. Kuner, D. Kuryla, G. Liepuoniute, J.T. Margraf, I.-B. Magdău, A. Michaelides, J.H. Moore, A.A. Naik, S.P. Niblett, S.W. Norwood, N. O'Neill, C. Ortner, K.A. Persson, K. Reuter, A.S. Rosen, L.L. Schaaf, C. Schran, E. Sivonxay, T.K. Stenczel, V. Svahn, C. Sutton, C. van der Oord, E. Varga-Umbrich, T. Vegge, M. Vondrák, Y. Wang, W.C. Witt, F. Zills, G. Csányi, A foundation model for atomistic materials chemistry, 2023, arXiv preprint arXiv:2401.00096.

[45] T. Liang, K. Xu, E. Lindgren, Z. Chen, R. Zhao, J. Liu, E. Berger, B. Tang, B. Zhang, Y. Wang, K. Song, P. Ying, N. Xu, H. Dong, S. Chen, P. Erhart, Z. Fan, T. Ala-Nissila, J. Xu, Nep89: Universal neuroevolution potential for inorganic and organic materials across 89 elements, 2025, arXiv preprint arXiv:2504.21286.

[46] B.M. Wood, M. Dzamba, X. Fu, M. Gao, M. Shuaibi, L. Barroso-Luque, K. Abdelmaqsoud, V. Gharakhanyan, J.R. Kitchin, D.S. Levine, K. Michel, A. Sriram, T. Cohen, A. Das, A. Rizvi, S.J. Sahoo, Z.W. Ulissi, C.L. Zitnick, Uma: A family of universal models for atoms, 2025, arXiv preprint arXiv:2506.23971.

[47] M. Čák, T. Hammerschmidt, J. Rogal, V. Vitek, R. Drautz, Analytic bond-order potentials for the bcc refractory metals nb, ta, mo and w, J. Phys.: Condens. Matter. 26 (2014) 195501.

[48] M.S. Nitol, D.E. Dickel, C.D. Barrett, Machine learning models for predictive materials science from fundamental physics: An application to titanium and zirconium, Acta Mater. 224 (2022) 117347.

[49] A.A. Kistanov, I.V. Kosarev, S.A. Shcherbinin, A.V. Shapeev, E.A. Korznikova, S.V. Dmitriev, Unified approach to generating a training set for machine learning interatomic potentials: The case of bcc tungsten, Mater. Today Commun. 42 (2025) 111437.

[50] I. Kosarev, S. Shcherbinin, A. Kistanov, R. Babicheva, E. Korznikova, S. Dmitriev, An approach to evaluate the accuracy of interatomic potentials as applied to tungsten, Comput. Mater. Sci. 231 (2024) 112597.

[51] P.-W. Ma, S. Dudarev, Effect of stress on vacancy formation and migration in body-centered-cubic metals, Phys. Rev. Mater. 3 (2019a) 063601.

[52] P.-W. Ma, S. Dudarev, Universality of point defect structure in body-centered cubic metals, Phys. Rev. Mater. 3 (2019) 013605.

[53] F.H. Featherston, J. Neighbours, Elastic constants of tantalum, tungsten, and molybdenum, Phys. Rev. 130 (1963) 1324.

[54] A. Dewaele, P. Loubeyre, M. Mezouar, Refinement of the equation of state of tantalum, Phys. Rev. B 69 (2004) 092106.

[55] C. Kittel, P. McEuen, Introduction To Solid State Physics, John Wiley & Sons, 2018.

[56] J.R. Morris, C. Wang, K. Ho, C.T. Chan, Melting line of aluminum from simulations of coexisting phases, Phys. Rev. B 49 (1994) 3109.

[57] A.B. Belonoshko, L.S. Dubrovinsky, Molecular dynamics of nacl (b1 and b2) and mgo (b1) melting; two-phase simulation, Am. Mineral. 81 (1996) 303–316.

[58] P.A.T. Olsson, P. Hiremath, S. Melin, Atomistic investigation of the impact of phosphorus impurities on the tungsten grain boundary decohesion, Comput. Mater. Sci. 219 (2023) 112017.

[59] H. Zheng, X.-G. Li, R. Tran, C. Chen, M. Horton, D. Winston, K.A. Persson, S.P. Ong, Grain boundary properties of elemental metals, Acta Mater. 186 (2020) 40–49.

[60] C. Li, S. Lu, S. Divinski, L. Vitos, Theoretical and experimental grain boundary energies in body-centered cubic metals, Acta Mater. 255 (2023) 119074.

[61] P. Grigorev, L. Frérot, F. Birks, A. Gola, J. Golebiowski, J. Grießer, J.L. Hörmann, A. Klemenz, G. Moras, W.G. Nöhring, J.A. Oldenstaedt, P. Patel, T. Reichenbach, T. Rocke, L. Shenoy, M. Walter, S. Wengert, L. Zhang, J.R. Kermode, L. Pastewka, matscipy: materials science at the atomic scale with Python, J. Open Source Softw. 9 (2024) 5668.

[62] L. Dezerald, L. Ventelon, E. Clouet, C. Denoual, D. Rodney, F. Willaime, Ab initio modeling of the two-dimensional energy landscape of screw dislocations in bcc transition metals, Phys. Rev. B 89 (2014) 024104.

[63] C. Kittel, Introduction To Solid State Physics, Wiley, New York, 2005.

[64] B.-T. Wang, P. Zhang, H.-Y. Liu, W.-D. Li, P. Zhang, First-principles calculations of phase transition, elastic modulus, and superconductivity under pressure for zirconium, J. Appl. Phys. 109 (2011) 063514.

[65] P. Souvatzis, O. Eriksson, M. Katsnelson, Anomalous thermal expansion in α-titanium, Phys. Rev. Lett. 99 (2007) 015901.

[66] T. Wen, R. Wang, L. Zhu, L. Zhang, H. Wang, D.J. Srolovitz, Z. Wu, Specialising neural network potentials for accurate properties and application to the mechanical response of titanium, Npj Comput. Mater. 7 (2021) 206.

[67] E. Fisher, C. Renken, Single-crystal elastic moduli and the hcp → bcc transformation in ti, zr, and hf, Phys. Rev. 135 (1964) A482.

[68] G. Simmons, H. Wang, Single crystal elastic constants and caluculated aggregate properties, in: A Handbook, second ed., 1971.

[69] C. Varvenne, O. Mackain, E. Clouet, Vacancy clustering in zirconium: An atomic-scale study, Acta Mater. 78 (2014) 65–77.

[70] D. Dickel, D. Francis, C. Barrett, Neural network aided development of a semi-empirical interatomic potential for titanium, Comput. Mater. Sci. 171 (2020) 109157.

[71] G.D. Samolyuk, A.V. Barashev, S.I. Golubov, Y. Osetsky, R.E. Stoller, Analysis of the anisotropy of point defect diffusion in hcp zr, Acta Mater. 78 (2014) 173–180.

[72] W. Tyson, W. Miller, Surface free energies of solid metals: Estimation from liquid surface tension measurements, Surf. Sci. 62 (1977) 267–276.

[73] Y. Udagawa, M. Yamaguchi, H. Abe, N. Sekimura, T. Fuketa, Ab initio study on plane defects in zirconium–hydrogen solid solution and zirconium hydride, Acta Mater. 58 (2010) 3927–3938.

[74] P.A.T. Olsson, M. Mrovec, M. Kroon, First principles characterisation of brittle transgranular fracture of titanium hydrides, Acta Mater. 118 (2016) 362–373.

[75] O.G. Nicholls, D.G. Frost, V. Tuli, J. Smutna, M.R. Wenman, P.A. Burr, Transferability of zr-zr interatomic potentials, J. Nucl. Mater. 584 (2023) 154391.

[76] J. Goldak, L. Lloyd, C. Barrett, Lattice. parameters, thermal. expansions, And grüneisen coefficients of zirconium, 4.2 to 1130 k, Phys. Rev. 144 (1966) 478.

[77] P. Mal'ko, D. Arensburger, V. Pugin, V. Nemchenko, S. L'vov, Thermal and electrical properties of porous titanium, Sov. Powder Met. Met. Ceram. 9 (1970) 642–644.

[78] S.A. Etesami, M. Laradji, E. Asadi, Reliability of molecular dynamics interatomic potentials for modeling of titanium in additive manufacturing processes, Comput. Mater. Sci. 184 (2020) 109883.

[79] J. Liu, L. Zhang, A physics-informed machine learning perspective to present the structures and properties of titanium matrixes and nanoclusters through atomic modeling, Nanoscale (2025).

[80] A. Efimov, L. Belorukova, I. Vasilkova, V. Chechev, Properties of Inorganic Compounds, Reference Book, Khimiya, Leningrad, 1983.

[81] A. Heiming, W. Petry, J. Trampenau, W. Miekeley, J. Cockcroft, The temperature dependence of the lattice parameters of pure bcc zr and bcc zr-2 at.% co, J. Phys.: Condens. Matter. 4 (1992) 727.

[82] V.N. Korobenko, A.I. Savvatimskii, Zirconium temperature measurements from the melting point to 4100 k involving the use of blackbody models in the liquid state, High Temp. 39 (2001) 485–490.

[83] J. Zhang, Y. Zhao, C. Pantea, J. Qian, L.L. Daemen, P.A. Rigg, R.S. Hixson, C.W. Greeff, III. G. T. Gray, Y. Yang, et al., Experimental constraints on the phase diagram of elemental zirconium, J. Phys. Chem. Solids 66 (2005) 1213–1219.

[84] H. Kleykamp, Highlights of experimental thermodynamics in the field of nuclear fuel development, J. Nucl. Mater. 344 (2005) 1–7.

[85] X.-G. Lu, M. Selleby, B. Sundman, Assessments of molar volume and thermal expansion for selected bcc, fcc and hcp metallic elements, Calphad 29 (2005) 68–89.

[86] J.S. Pigott, N. Velisavljevic, E.K. Moss, N. Draganic, M.K. Jacobsen, Y. Meng, R. Hrubiak, B.T. Sturtevant, Experimental melting curve of zirconium metal to 37 gpa, J. Phys.: Condens. Matter. 32 (2020) 355402.

[87] H.B. Radousky, M.R. Armstrong, R.A. Austin, E. Stavrou, S. Brown, A.A. Chernov, A.E. Gleason, E. Granados, P. Grivickas, N. Holtgrewe, et al., Melting and refreezing of zirconium observed using ultrafast x-ray diffraction, Phys. Rev. Res. 2 (2020) 013192.

[88] S. Singhal, W. Worrell, High temperature thermodynamic properties of solid ta-w alloys, Met. Trans. 4 (1973) 895–898.

[89] A.F. Guillermet, Phase diagram and thermochemical properties of the zr-ta system. an assessment based on gibbs energy modelling, J. Alloys Compd. 226 (1995) 174–184.

[90] R. Chinnappan, B. Panigrahi, A. van de Walle, First-principles study of phase equilibrium in ti–v, ti–nb, and ti–ta alloys, Calphad 54 (2016) 125–133.

[91] P. Lafaye, C. Toffolon-Masclet, J.-C. Crivello, J.-M. Joubert, Experimental investigations and thermodynamic modelling of the cr–nb–sn–zr system, Calphad 64 (2019) 43–54.
[92] M. Chandran, P. Subramanian, M.F. Gigliotti, First principles calculation of mixing enthalpy of β-ti with transition elements, J. Alloys Compd. 550 (2013) 501–508.
[93] D. Shin, R. Arróyave, Z.-K. Liu, A. Van de Walle, Thermodynamic properties of binary hcp solution phases from special quasirandom structures, Phys. Rev. B—Condensed Matter Mater. Phys. 74 (2006) 024204.
[94] R.J. Perez, B. Sundman, Thermodynamic assessment of the mo–zr binary phase diagram, Calphad 27 (2003) 253–262.
[95] P. Zhou, Y. Peng, Y. Du, S. Wang, G. Wen, Thermodynamic modeling of the c–w–zr system, Int. J. Refract. Met. Hard Mater. 50 (2015) 274–281.
[96] I.A. Ditenberg, I.V. Smirnov, M.A. Korchagin, K.V. Grinyaev, V.V. Melnikov, Y.P. Pinzhin, A.I. Gavrilov, M.A. Esikov, V.I. Mali, D.V. Dudina, Structure and phase composition of a w-ta-mo-nb-v-cr-zr-ti alloy obtained by ball milling and spark plasma sintering, Entropy 22 (2020) 143.
[97] M. Bönisch, A. Panigrahi, M. Stoica, M. Calin, E. Ahrens, M. Zehetbauer, W. Skrotzki, J. Eckert, Giant thermal expansion and α-precipitation pathways in ti-alloys, Nat. Commun. 8 (2017) 1429.
[98] J.G. Moreno, M. Bönisch, N. Panagiotopoulos, M. Calin, D. Papageorgiou, A. Gebert, J. Eckert, G. Evangelakis, C.E. Lekka, Ab-initio and experimental study of phase stability of ti-nb alloys, J. Alloys Compd. 696 (2017) 481–489.
[99] F. Stein, A. Leineweber, Laves phases: a review of their functional and structural applications and an improved fundamental understanding of stability and properties, J. Mater. Sci. 56 (2021) 5321–5427.
[100] J.E. Saal, S. Kirklin, M. Aykol, B. Meredig, C. Wolverton, Materials design and discovery with high-throughput density functional theory: the open quantum materials database (oqmd), Jom 65 (2013) 1501–1509.
[101] S. Kirklin, J.E. Saal, B. Meredig, A. Thompson, J.W. Doak, M. Aykol, S. Rühl, C. Wolverton, The open quantum materials database (oqmd): assessing the accuracy of dft formation energies, Npj Comput. Mater. 1 (2015) 1–15.
[102] J.-P. Crocombette, Influence of charge states on energies of point defects and clusters in uranium dioxide, Phys. Rev. B—Condensed Matter Mater. Phys. 85 (2012) 144101.
[103] S. Starikov, M. Korneva, Description of phase transitions through accumulation of point defects: Un, uo2 and uc, J. Nucl. Mater. 510 (2018) 373–381.
[104] V. Kocevski, D.A. Rehn, M.W. Cooper, D.A. Andersson, First-principles investigation of uranium mononitride (un): Effect of magnetic ordering, spin–orbit interactions and exchange correlation functional, J. Nucl. Mater. 559 (2022) 153401.
[105] J. Zhu, L. Pike, C. Liu, P. Liaw, Point defects in binary laves phase alloys, Acta Mater. 47 (1999) 2003–2018.
[106] J. Guénolé, F.-Z. Mouhib, L. Huber, B. Grabowski, S. Korte-Kerzel, Basal slip in Laves phases: the synchroshear dislocation, Scr. Mater. 166 (2019) 134–138.
[107] Z. Xie, D. Chauraud, A. Atila, E. Bitzek, S. Korte-Kerzel, J. Guénolé, Thermally activated nature of synchro-Shockley dislocations in Laves phases, Scr. Mater. 235 (2023) 115588.
[108] G. Henkelman, B.P. Uberuaga, H. Jónsson, A climbing image nudged elastic band method for finding saddle points and minimum energy paths, J. Chem. Phys. 113 (2000) 9901–9904.
[109] G. Henkelman, H. Jónsson, Improved tangent estimate in the nudged elastic band method for finding minimum energy paths and saddle points, J. Chem. Phys. 113 (2000) 9978–9985.
[110] Z. Xie, D. Chauraud, A. Atila, E. Bitzek, S. Korte-Kerzel, J. Guénolé, Unveiling the mechanisms of motion of synchro-Shockley dislocations in Laves phases, Phys. Rev. Mater. 7 (2023) 053605.
[111] M.F. Chisholm, S. Kumar, P. Hazzledine, Dislocations in complex materials, Science 307 (2005) 701–703.
[112] W. Zhang, R. Yu, K. Du, Z. Cheng, J. Zhu, H. Ye, Undulating slip in laves phase and implications for deformation in brittle materials, Phys. Rev. Lett. 106 (2011) 165505.
[113] Y. Chai, H. Kim, H. Hosoda, S. Miyazaki, Self-accommodation in ti–nb shape memory alloys, Acta Mater. 57 (2009) 4054–4064.
[114] H.Y. Kim, J. Fu, H. Tobe, J.I. Kim, S. Miyazaki, Crystal. structure, transformation. strain, And superelastic property of ti–nb–zr and ti–nb–ta alloys, Shape Mem. Superelasticity 1 (2015) 107–116.
[115] A. Konopatsky, S. Dubinskiy, Y.S. Zhukova, V. Sheremetyev, V. Brailovski, S. Prokoshkin, M. Filonov, Ternary ti-zr-nb and quaternary ti-zr-nb-ta shape memory alloys for biomedical applications: Structural features and cyclic mechanical properties, Mater. Sci. Eng.: A 702 (2017) 301–311.